Oriented porous LLZO 3D structures obtained by freeze casting for battery applications

Journal:	*Journal of Materials Chemistry A*
Manuscript ID	TA-ART-06-2019-006520.R1
Article Type:	Paper
Date Submitted by the Author:	16-Aug-2019
Complete List of Authors:	Shen, Hao; Lawrence Berkeley National Laboratory, Energy Storage and Distributed Resources Division; Xi'an Jiaotong University, Center for Advancing Materials Performance from the Nanoscale (CAMP-Nano), State Key Laboratory for Mechanical Behavior of Materials Yi, Eongyu; Lawrence Berkeley National Laboratory, Energy Storage and Distributed Resources Division Amores, Marco; The University of Tokyo Cheng, Lei; Lawrence Berkeley National Laboratory, Energy Storage and Distributed Resources Division; Robert Bosch LLC Research and Technology Center North America Tamura, Nobumichi; Lawrence Berkeley National Laboratory, Advanced Light Source Parkinson, Dilworth; Lawrence Berkeley National Laboratory, Advanced Light Source Chen, Guoying; Lawrence Berkeley National Laboratory, Energy Storage and Distributed Resources Chen, Kai; Xi'an Jiaotong University, Center for Advancing Materials Performance from the Nanoscale (CAMP-Nano), State Key Laboratory for Mechanical Behavior of Materials Doeff, Marca; Lawrence Berkeley National Laboratory, Energy Storage and Distributed Resources Division

1   Oriented porous LLZO 3D structures obtained by freeze

2   casting for battery applications

3

4   Hao Shen,[a,b] Eongyu Yi,[b] Marco Amores,[b,c] Lei Cheng,[b,d] Nobumichi Tamura,[e] Dilworth Y.

5   Parkinson,[e] Guoying Chen,[b] Kai Chen,[a] and Marca Doeff [b]

6   a) Center for Advancing Materials Performance from the Nanoscale (CAMP-Nano), State Key

7   Laboratory for Mechanical Behavior of Materials, Xi'an Jiaotong University, Xi'an, Shaanxi

8   710049, China

9   E-mail: kchenlbl@gmail.com

10   b) Energy Storage and Distributed Resources Division, Lawrence Berkeley National Laboratory,

11   Berkeley, CA 94720, USA

12   E-mail: mmdoeff@lbl.gov

13   c) Department of Chemistry, Graduate School of Science, The University of Tokyo, 7-3-1,

14   Hongo, Bunkyo-Ku, Tokyo, 113-0033, Japan

15   d) Robert Bosch LLC, Research and Technology Center, Sunnyvale, CA 94085, USA

16   e) Advanced Light Source, Lawrence Berkeley National Laboratory, Berkeley, CA 94720, USA

17

18   **Abstract**

19   All solid-state lithium batteries are, potentially, higher energy density and safer alternatives

20   to conventional lithium-ion batteries (LIBs). These are particularly attractive characteristics for

21   large-scale applications such as electric vehicles and grid energy storage systems. However, the

22   thin film deposition techniques used to make current devices are not readily scalable, and result in

23   low areal capacities, which translate to low practical energy densities. To overcome these

24   deficiencies, it is necessary to design thicker electrodes similar to what are used in LIBs (30-100

25   μm), in which active material is composited with the ionic conductor and an electronically

26   conducting additive, to overcome transport limitations. In this paper, we propose a method for

27   making such an electrode, starting with a porous scaffold of $Li_7La_3Zr_2O_{12}$ (LLZO), made by freeze

28   casting, which is then infiltrated with active material $LiNi_{0.6}Mn_{0.2}Co_{0.2}O_2$ (NMC-622) and other

29   components. The freeze casting technique results in the formation of oriented channels with low

30   tortuosity, which run roughly parallel to the direction of current. The scaffolds were characterized

31   with synchrotron X-ray micro-tomography for structural analysis, as well as synchrotron X-ray

32   fluorescence to map the elemental distribution in the infiltrated composite. A hybrid half-cell was

33   constructed and cycled as proof of principle, and showed good stability. In addition, a bilayer

34   structure consisting of a porous layer combined with a dense LLZO film was successfully made

35   as a prototype of an all solid-state battery. A mathematical model was established to propose

36   optimized scaffold structures for battery performance.

Introduction

The widespread use of Li-ion batteries (LIBs) in electronic devices and electric vehicles has highlighted the need for both improved safety and energy density. The use of lithium metal as an anode can potentially increase both specific energy and energy density due to the high gravimetric capacity (3869 mAh/g) and low density (0.534 g/cm^3).[1-3] Unfortunately, safety issues preclude its use in conventional battery configurations because of mossy lithium deposition or Li-dendrite induced cell shorting when Li metal is cycled in cells with flammable liquid electrolytic solutions.[4] To overcome this, solid state electrolytes have been proposed as safer alternatives to the liquids. In particular, solid-state garnet type ceramic electrolytes, such as cubic Al-substituted Li$_7$La$_3$Zr$_2$O$_{12}$ (LLZO), are promising, due to their kinetic stability against Li,[5-8] large potential window (0 ~ 6V), and ionic conductivities up to 1 mS/cm.[9-15] Although Li deposition or dendrite growth along the LLZO grain boundaries in polycrystalline dense films has recently been recognized as a source of shorting in cells, modifications of the LLZO/Li interface and cell architecture have successfully improved the stability and cycling behavior of symmetrical cells.[11, 16-19]

Another challenge, particularly if solid-state batteries are to be used for large-scale applications such as vehicles, has to do with the design of the electrodes and cells.[20] Most solid-state batteries are fabricated in thin film configurations to overcome the transport limitations of cathode materials.[21-24] Not only does this usually requires the use of vacuum deposition techniques, which are costly and difficult to scale, but it also results in low cathode areal capacity. For this reason, practical energy densities are low, in spite of the use of metallic lithium anodes. Several attempts have been made to build composite electrodes for solid-state batteries, in which the active material and ionic conductor are combined to improve ionic transport. In some cases, composites

60   may be fabricated by cold-pressing the active material and electrolyte together[25-27]. This is most

61   easily accomplished with soft electrolytes such as sulfides. The low compressibility of garnets, in

62   contrast, makes this an impractical approach. Instead, Fu *et al.* constructed a porous garnet layer

63   by including a sacrificial polymer, which was burned away to create pores and then infiltrated

64   these with other components to make a composite.[28]

65   Sander *et al* recently demonstrated the advantages of low tortuosity pores in battery

66   electrodes using a magnetic alignment technique on thick $LiCoO_2$ electrodes.[29] There was a

67   noticeable increase of usable capacity of the aligned $LiCoO_2$ electrodes with low tortuosity pores

68   oriented in the direction of transport, compared to those with isotropic porosity, when cycled in

69   half cells with liquid electrolytic solutions. To this end, McOwen *et al.* 3D printed LLZO scaffolds

70   by using LLZO inks, which allows good control of the electrode structure.[30] The effect of tortuosity

71   on the electrochemical behavior of LLZO electrolytes has recently been described, with lower

72   tortuosity potentially providing a means for achieving higher critical current densities and power

73   densities in solid-state batteries[31]. Another attractive method for producing low-tortuosity pores in

74   ceramics is that of freeze casting.[32] There has already been a report on freeze-casting LLZO to

75   make ceramic/polymer composite electrolytes[33]. Here we report our preliminary results using

76   freeze casting to produce LLZO scaffolds with low tortuosity pores, which were subsequently

77   infiltrated with active material and used as electrodes in hybrid half-cells. A prototype all solid-

78   state cell was also assembled. We used synchrotron radiation micro-computed tomography to

79   visualize the three-dimensional (3D) models of the porous LLZO scaffolds and X-ray fluorescence

80   to map distributions of the components. A simple mathematical model is also presented to provide

81   guidance on the design of the porous scaffolds.

82

Experimental

1. Preparation of porous LLZO scaffolds

Sub-micron-sized commercial Al-doped LLZO powders were obtained from MSE Supplies, Inc. for the freeze casting experiments. A slurry containing 20 wt.% LLZO powder and 78 wt.% tert-butyl alcohol (TBA) was mixed with 1 wt.% polyvinyl butyral (PVB) and 1 wt.% deionized water (to adjust the freezing point). Afterwards, another 5 wt.% Li_2CO_3 was added into the slurry to compensate for Li loss during sintering. The mixture was ball-milled with ZrO_2 grinding media for 8 h to form a stable LLZO slurry at room temperature. Although water is known to cause slow decomposition of LLZO, the amount of decomposed LLZO is negligible after several hours ball milling. Moreover, during the sintering process, the decomposed LLZO is recovered through addition of extra Li_2CO_3 and heating. A house-made freeze casting system was used to prepare samples at various temperatures as illustrated in Figure 1a. A PVC mold of 2 cm in diameter and 1.5 cm in height was attached to a liquid nitrogen cooling bed with a polished copper plate in between to ensure excellent thermal conductivity. The top surface of the slurry is still exposed to ambient temperature resulting in a temperature gradient from the bottom (cold) to the top (warm). To control the freezing rate, the temperature of the slurry was adjusted and monitored by an embedded heating element and thermocouple in the cooling bed. For this work, the cooling plate temperature was set at -20 °C and -50 °C. After the temperature stabilized, the LLZO slurry was poured into the mold and maintained at the desired temperature until fully frozen. Then the solidified TBA and LLZO was unmolded and transferred to a freeze drier at -40 °C and kept under vacuum overnight to sublime the TBA crystals (Figure 1b). The removal of TBA through this process results in a porous green body structure (inset of Figure 1b). Some samples were also prepared using water as the solvent as follows: 15-30 wt. % LLZO, was mixed with 1 wt.% Darvan,

106   1 wt.% Poly(vinyl alcohol) (PVA) and the remainder deionized water, then ball milled overnight

107   and frozen at a cooling rate about of ~20 °C/min. One sample was also prepared substituting gelatin

108   for PVA.

109   The scaffolds were then sintered at 1050 °C for 2 h in Ar atmosphere. Ambient air was

110   avoided because a large amount of lithium was lost, resulting in decomposition of the LLZO and

111   crumbling of the structure (SI, Figure S1). The sintered scaffolds decreased in volume substantially

112   (inset of Figure 1b). The scaffolds were then encapsulated with epoxy (Allied High Tech Products,

113   Inc.) to avoid destroying the scaffold during the following operations, which had an insignificant

114   volume change after curing, and sliced into thin sections using a diamond saw. The LLZO section

115   with thickness of 200 μm showed high optical transparency (Figure 1c). Freestanding porous

116   LLZO scaffold films were obtained after burning away the epoxy in dry air at 800 °C for 30 min.

117   **2. Preparation of dense/porous LLZO bilayer structures**

118   The oriented scaffold becomes fragile and hard to handle after sintering, especially when

119   sliced thin. Adding PVDF binder into the NMC slurry helps to keep the integrity of the composite

120   electrode. Another solution to avoid damage and fracture during assembly is to support the porous

121   layers with a dense layer to form a bilayer structure. In this study, two types of dense LLZO

122   structures with thicknesses of approximately 100 μm and 20 μm were used for the proof of

123   principle study and the prototype half-cells, respectively. The thick dense films were fabricated

124   using a tape casting method. The LLZO slurry for the dense layer preparation was a mixture of 30

125   wt.% LLZO powders, 3 wt.% Li_2CO_3 (32 wt.% extra elemental Li in LLZO), 3 wt.% PVA and 64

126   wt.% analytically pure isopropyl alcohol. The slurry was introduced into a ZrO_2 container and ball

127   milled with ZrO_2 milling media using a SPEX 8000M mixer for 30 minutes to guarantee a stable

128   suspension of LLZO. Then the slurry was tape cast onto conventional household polyethylene

129   membranes using a doctor blade, and dried at room temperature. The dried LLZO film was peeled

130   off the polyethylene membrane, cut into pieces and cold pressed using a stainless-steel die.

131   The ultrathin LLZO dense films (~20 μm thick) were fabricated adopting a previously

132   reported approach.[34] LLZO, Li_2CO_3, polyvinyl butyral (binder), and benzyl butyl phthalate

133   (plasticizer) were dissolved/dispersed in an alcohol/acetone mixed solvent system by ball-milling

134   for 48 h using 3 mm ZrO_2 beads. The suspension was formulated to result in ~55 vol.%

135   LLZO/Li_2CO_3 excluding the solvent. The amount of Li_2CO_3 was selected to equal 50 wt.% excess

136   elemental Li in LLZO. The suspension was tape cast onto a Mylar substrate and left to dry for

137   several hours. The dried green tapes were peeled off and punched to desired sizes for subsequent

138   sintering.

139   The bilayer structure was prepared by co-sintering a LLZO porous scaffold (after epoxy

140   burnout) and a dense film (green) at 1070 °C for 3 h in Ar atmosphere between two pieces of

141   alumina disks, each of which was 2 mm thick. No extra pressure was imposed onto the LLZO

142   scaffold and film besides the weight of the alumina disks. In order to prevent unwanted diffusion

143   and reaction with the alumina, graphite foils or Ni meshes were placed between the LLZO and the

144   disks.

145   **3. Active material infiltration and electrochemical testing**

146   In this study, the NMC-622 particles (3-12 μm) provided by Umicore, Inc. were introduced

147   into the LLZO scaffolds as the active material. A slurry was prepared by mixing 84 wt.% NMC-

148   622, 8 wt.% carbon black, and 8 wt.% PVDF into N-methyl-2-pyrrolidone (NMP). During the

149   stirring, several more drops of NMP were added to adjust the viscosity of the slurry. The slurry

150   was then drop-cast onto the LLZO scaffolds. The success of the infiltration process of NMC

151   particles could be readily indicated by a color change from natural ivory to black. It usually took

152 several rounds of infiltration to fully fill the pores, as confirmed by scanning electron microscope

153 (SEM) observation of the bottom surface of the infiltrated sample. The addition of polyaniline was

154 also demonstrated in freeze cast structures (see SI, Figure S2e). A partially infiltrated sample was

155 also prepared using smaller (submicron in diameter) NMC particles (SI, Figure S3). Smaller NMC

156 particles were obtained by ball-milling the as-received NMC for 48 h in EtOH using 2 mm ZrO_2

157 beads which resulted in fracturing of secondary particles to primary particles. After infiltration,

158 samples were kept in a vacuum oven at 80 °C overnight.

159 The composite structures were then transferred to an Argon-filled glove box for assembly

160 into coin cells. For the hybrid cells, Celgard 2400 polypropylene membranes wet with 1 M $LiPF_6$

161 in ethylene carbonate : diethyl carbonate (1 : 1 vol%) were employed as separators, and Li foils

162 (Alfa-Aesar) were used as the anodes. The coin cells were then galvanostatically cycled using a

163 VMP3 multichannel potentiostat/galvanostat equipped with a frequency response analyzer

164 between 2.5 and 4.7 V at a current density of 0.3 mA/cm^2 (approximately a ten hour rate) after 12

165 hours rest. The impedance was measured from 1 mHz to 100 kHz every 10 cycles. The bilayer

166 structures were also assembled into coin cells with lithium anodes, without polymeric separators

167 or liquid electrolyte. The open circuit voltage was monitored for 12 h.

168 **4. Structure characterization**

169 The morphologies of the selected samples were examined using a Hitachi TM-1000

170 tabletop scanning electron microscope (SEM). Filters were applied to binarize the SEM images

171 (SI, Figure S4) to enable measurement of pore size and estimate porosity by calculating the dark

172 area. X-ray powder diffraction (XRD) patterns were acquired on a Bruker D2 PHASER

173 diffractometer with monochromatic Cu K_α radiation to check the phase purity of the samples.

174   Because of the fragility of the LLZO samples after sintering, the freeze cast pellet was first

175   mounted in epoxy prior to sample characterization. Both the LLZO films and longitudinal sections

176   were cut from the same sample. Films were cut perpendicular to the TBA channel growing

177   direction, while the longitudinal sections were cut parallel to the channel direction. The thicknesses

178   of the films and the diameters of the longitudinal sections were controlled to be 200-300 μm. Then

179   synchrotron micro computed tomography (SR-μCT) experiments were performed at Hard X-ray

180   Micro-Tomography Beamline 8.3.2 of the Advanced Light Source (ALS) on the samples. Images

181   were collected over 180 degrees in 0.072 degree steps, with 24 keV X-rays. Detection was

182   accomplished with a 50 micrometer thick LuAG:Ce scintillator, a 10x Olympus optical lens in an

183   optical system from Optique Peter, and a PCO.edge sCMOS detector, with 500 ms exposure time.

184   Dark field images (with the X-ray shutter closed) were collected to subtract detector dark counts,

185   and bright field images were collected before and after the sample scan to normalize for variations

186   in the incident illumination. The voxel dimension with this setup was approximately 0.64 microns.

187   Tomographic reconstruction was done with TomoPy[35] and Xi-CAM[36]. Visualization and analysis

188   was done with Avizo, from FEI.

189   The elemental distribution of the NMC particle-infiltrated LLZO scaffolds was mapped

190   using the synchrotron radiation based X-ray micro-fluorescence (SR-μXRF) technique, which was

191   conducted at Beamline 12.3.2 of the ALS. The specimen cross-section along the thickness

192   direction was raster scanned using a micro-focused polychromatic X-ray beam (5 – 24 keV). At

193   each scanning position the fluorescence signal was collected with a silicon drift detector. In this

194   study, the Zr K-edge and Mn K-edge intensities were recorded, and thus the concentration

195   distribution of these two elements were obtained.

196

Results and discussion

197

198   The fracture surface of a green body made using TBA frozen at -20 °C is shown in Figures

199   2a and b. The long channels exhibit clean and sharp edges, with minimal bridging. After sintering,

200   the structure shrank by about 35% in diameter and became fragile. The fracture surface of the

201   sintered scaffold in Figure 2c and d displays walls with high density and low thickness, composed

202   of grains about 2 μm in diameter. The walls in the scaffold are only a few grains thick, and the

203   pores are prismatic in shape and well faceted due to the directional growth behavior of the TBA.

204   The 3D image of the sintered scaffold was collected using SR-μCT. A sub-volume with

205   the size of 700 μm × 700 μm × 200 μm of the LLZO film is shown in Figure 3a. A video of the

206   reconstructed model is included in the supporting information, and one slice of the top view and

207   left view from this video are shown in Figures 3b and c, respectively, indicating that the pore size

208   is around 50 μm and that the pores are uniformly distributed throughout the whole structure. Better

209   contrast is obtained from the 3D model of a LLZO longitudinal section shown in Figure 3d. By

210   rotating the image, it is found that the smooth and empty channels with the same orientation are

211   present and there is no bridging over the length range of several hundred microns (Figures 3e and

212   f), which by far exceeds the thickness of the scaffolds (~100 μm). Moreover, the shape and size of

213   the channels remain comparatively unvaried throughout the thickness of the sample. The long-

214   range bridge-free structure provides distinct advantages for the infiltration process compared to

215   the slit-like or layer-stacked structures fabricated using water as the solvent for freeze casting (SI,

216   Figure S2, S5).

217   The temperature of the cooling bed in the freeze cast apparatus is one of the key processing

218   parameters for optimizing the pore size and porosity of the LLZO scaffold. A lower cooling

219   temperature leads to more nucleation sites and higher solidification velocity, and thus finer TBA

10

220 dendrites are formed, resulting in more, smaller pores than when the temperature is higher.

221 However, if the temperature is too low, the sample may crack; if it is too high, the slurry will not

222 freeze completely in a reasonable period of time. The SEM images of the top cross sections of

223 samples which are frozen at -20 and -50 $^{\circ}$C are compared in Figure 4. Both samples were sintered

224 before taking the SEM photos. The average pore size of the sample processed at -20 $^{\circ}$C is about

225 52 μm, twice as large as the one fabricated at -50 $^{\circ}$C (~23 μm). A statistical analysis of the white

226 (LLZO scaffold) and black areas (pores) indicates that the porosity of the -20 $^{\circ}$C sample is 73

227 vol.% and the -50 $^{\circ}$C sample has a lower porosity of about 60 vol.%. The same trend was also

228 reported by Xu et $al.$ in the freeze cast lead zirconate titanate (PZT) system.[37] As the cooling bed

229 temperature decreases, a higher volume fraction of pore walls form, and pore size decreases.

230 After the initial sintering but prior to epoxy burned out, the excess Li_2CO_3 used to

231 compensate for Li loss results in the formation of some tetragonal LLZO, evidenced by the weak

232 peak splitting observed in the XRD pattern (Figure 5a). After the epoxy removal heat treatment,

233 the tetragonal LLZO signals disappear and the structure fully converts to cubic LLZO, with traces

234 of $LiAlO_2$ and $La_2Zr_2O_7$ impurities associated with Li loss due to the high temperature exposure.

235 Although increasing the amount of excess of Li_2CO_3 helps to compensate for the Li loss, it also

236 accelerates the sintering process and generates cracks in the bulk of LLZO scaffold, which is

237 undesirable.

238 As the NMC particles are comparable in size to the pore size obtained at -50 $^{\circ}$C, the

239 infiltration would be challenging. Only a few point contacts would be formed between LLZO and

240 NMC, which is harmful to the cell performance. Thus, the scaffold made at -20 $^{\circ}$C is preferable

241 for cell testing. The bottom view of the LLZO scaffold freeze cast at -20 $^{\circ}$C infiltrated with NMC

242 particles, PVDF, and carbon suggests that a fraction of the pores are not completely filled (Figure

243   5b). A scaffold about 8 mm in diameter and 1 mm in thickness was infiltrated using the same

244   process and contains 7.9 mg NMC-622, corresponding to active material loading of 15.7 mg/cm^2

245   or about 3.14 mAh/cm^2 (based on the practical specific capacity of 200 mAh/g), similar to loadings

246   used in commercial lithium-ion batteries. It was then incorporated into a hybrid cell with Celgard

247   separator, electrolytic solution, and Li anode, and was cycled at a current density of 0.3 mA/cm^2

248   between 4.7 and 2.5V (approximately C/10). The charge and discharge profiles of every tenth

249   cycle as a function of cycle number are shown in Figure 6a, together with Coulombic efficiency

250   and capacity for each cycle (Figure 6b). The initial capacity of NMC-622 is similar to that of

251   previously reported values, which is around 200 mAh/g when charged to over 4.5 V.[38,39] The areal

252   capacity is also comparable to the reported high areal loading liquid Li/NMC-622 cell of about 3

253   mAh/cm^2 with current density of 0.5 mA/cm^2.[40,41] There is some capacity fading observed, but it

254   is similar to what is seen in conventional NMC half-cells cycled under similar conditions.[42] The

255   fading can be attributed to the increased interfacial impedance (Figure 6c) caused by the formation

256   of a resistive cathode/electrolyte film and surface reconstruction to rock salt, similar to what is

257   seen in the conventional cells. This has been documented in many reports using surface sensitive

258   characteristic techniques[39,42-46]. These results can be taken as proof of principle that infiltrated

259   scaffolds of LLZO can be used as cathodes in cells, although further optimization is required.

260   Although the specific area loading of the active material NMC demonstrated in this

261   example, 15.7 mg/cm^2, is fairly high, the pores are not completely filled using the drop casting

262   method. The density of NMC-622 provided by the manufacturer is about 2 g/cm^3. From the SEM

263   images, the porosity of the LLZO scaffold is estimated to be approximately 70% of the total

264   volume. Therefore, only 11% of the pore volume is filled by NMC-622. Thinner scaffolds, similar

265   to what is used in lithium ion batteries (about 1/10 of this thickness or ~100 μm) would be easier

266   to infiltrate and would most likely perform better, particularly if a completely solid state

267   configuration is used. Work on making thinner scaffolds and optimizing the infiltration process is

268   currently underway in our laboratories.

269   The ultimate goal is to use the scaffolds in a totally solid state configuration. To this end,

270   we built bilayer structures, in which a dense LLZO layer is stacked with a porous scaffold and

271   sintered together (Figure 7a). In other words, the dense LLZO layer is employed in this

272   configuration to play the role that both the separator and liquid electrolytic solution play in a hybrid

273   cell. From the XRD patterns in Figure 7b, fewer impurities are formed in the scaffold upon

274   sintering in a bilayer configuration than those shown in Figure 5a, because the dense layer acts as

275   an additional source of lithium. Figure 7c and d show the fracture surfaces of the bilayer structures

276   with 100 μm and 20 μm thick dense layers fabricated by the two different approaches explained

277   in the experimental section, respectively. In both structures, the porous scaffold is about 150 μm

278   thick. A smooth fracture surface will be formed if the scaffold and dense layer are well connected,

279   which is important for ion transfer. Combining the results from the SEM photos and the fracture

280   surfaces, it appears that the connections are partly formed, but there are still some gaps between

281   scaffold and dense layer, which may be caused by different shrinkage rates of the two parts during

282   the sintering procedure. The overall differences in shrinkage rates can be caused by the difference

283   in porosities and additive concentrations. In addition, once a local connection is formed, the area

284   around will be pinned (SI, Figure S6b), and the uneven shrinkage may result in gaps between the

285   layers and even pinholes in the dense layer (SI, Figure S6c). It can also be seen that the channels

286   in the scaffold are oriented slightly off the normal direction of the interface.

287   After the active material NMC-622 was infiltrated into the scaffold, the cross section

288   morphology of the bilayer structure was first observed in SEM in backscattered electron (BSE)

289   mode (Figure 7e), and then the elemental distribution was mapped using the SR-µXRF method,

290   focusing on the Mn K-edge signals arising from the NMC and the Zr K-edge signals from LLZO

291   (Figure 7f). The Mn signal is primarily located in the areas where Zr is absent and almost fills

292   these spaces, even though many of the NMC particles cannot be seen in the corresponding SEM

293   images. From the map as well as the SEM images, a thin layer of NMC particles are observed on

294   top of the scaffold after infiltration, indicating some heterogeneity in the distribution. A cell with

295   a lithium foil anode and bilayer with the 20 µm thick dense layer as separator was assembled and

296   the open circuit voltage (OCV) monitored over a period of about twelve hours (SI, Figure S7).

297   Initially, the OCV was close to 0V, indicating shorting of the cell. However, the potential rose to

298   2V over 2 hours, and then reached 2.8 V after 12 hours, the expected potential for a Li/NMC cell

299   in the discharged state. This indicates that there was a soft short that could have been caused by

300   pinholes in the dense film, which allowed some carbon particles to cross over and caused initial

301   voltage instability (SI, Figure S8). Although thicker dense layers might mitigate the soft short

302   problem, this would come at the cost of higher cell resistance and reduced energy density due to

303   the weight of the excess LLZO. Therefore, it remains a particular challenge when very thin dense

304   layers are used in solid-state configurations along with extremely fine particles of carbon. The tri-

305   layer LLZO reported by G. T. Hitz *et al.* offers a successful example for densifying multi-layer

306   LLZO structures through laminating green LLZO layers as porous-dense-porous sandwich

307   structures[47]. This method decreases the difference in shrinkage rates between the scaffolds and

308   dense layers and also balances the stresses on both sides. However, for the porous structure made

309   by freeze casting in the current study, the bulk scaffold needed to be sliced into thin sections, and

310   the fragile ceramic structure needed to be stabilized. Thus sintering the structure for a short time

311   was required. We are currently exploring making trilayers and using a related technique, which

312   yields thinner structures (freeze tape casting), and which will simplify this process.

313   A number of technical questions arise for this approach. The oriented low-tortuosity

314   channels in the freeze cast scaffolds should be advantageous because they minimize ion diffusion

315   distances, but it is not clear what the optimized channel sizes, wall thicknesses, and porosities

316   should be. To attempt to answer these questions, we established a simple model for semi-

317   quantitative estimations of these parameters. For the model, the geometric configuration of the

318   porous scaffold shown in Figure 8a was assumed. The channels are assumed to run through the

319   thickness of the scaffold and have smooth walls, have the same constant diameter, and are

320   uniformly distributed with no bridges to form a regular hexagonal honeycomb. The top view in

321   Figure 8b shows the various parameters such as the pore diameter (d_p), wall thickness (d_w), porosity,

322   and number density of the pores. Taking the number density of the pores as N (per unit area), the

323   side length a (distance between centers of adjacent pores) of the regular hexagonal base is

324   calculated to be:

325
$$a = \left(\frac{2}{\sqrt{3}} \frac{1}{N} \right)^{1/2} \qquad (1)$$

326   For a scaffold with the porosity P, the diameter of the pores d_p and the wall thickness d_w

327   are:

328
$$d_p = \left(\frac{4P}{\pi N} \right)^{1/2} = \left(\frac{2\sqrt{3}P}{\pi} \right)^{1/2} \cdot a \qquad (2)$$

329   and

330
$$d_w = a - d_p = \left[1 - \left(\frac{2\sqrt{3}P}{\pi} \right)^{1/2} \right] \cdot a, \qquad (3)$$

331 respectively. It is self-evident that for higher porosities in the structure, more active material can

332 be infiltrated into the channels resulting in higher areal capacity. However, Equation (3) suggests

333 that the porosity cannot be close to 100%. Even when the wall thickness is infinitesimally small,

334 LLZO will be left at the corners of the hexagons shown in Figure 8b to maintain the integrity of

335 the scaffold, and a theoretically maximal porosity, $P_{max} = \dfrac{\pi}{2\sqrt{3}} = 91\%$, will be obtained.

336 When using this type of scaffold structure with active material infiltrated into the channels,

337 which run approximately parallel to the current direction, the lithium diffusion path length is

338 shortened and effective NMC/LLZO contact area is increased, compared to the case in which dense

339 LLZO films are employed. A semi-quantitative evaluation of the improved performance is

340 estimated. Considering that Li ions diffuse in LLZO and in the active material at different rates,

341 we can define a constant K as the diffusivity ratio: $K = \dfrac{D_{LLZO}}{D_{cathode}}$. From Einstein's random walk

342 theory[48], we know that in a certain period of time the Li ion diffusion distance in LLZO and in the

343 active material follow a square root relationship. In other words, in the same period of time, Li

344 ions will migrate the length L_{NMC} in NMC as $\sqrt{K} \cdot L_{NMC}$ in LLZO. The equivalent Li ion diffusion

345 path in the porous/dense bilayer structure $L_{bilayer}$, assuming that the channels are all fully infiltrated

346 by active materials, and that Li ions need to first diffuse from NMC to LLZO and then migrate

347 through LLZO, is expressed as:

348
$$L_{bilayer} = \int_0^{t_s} \int_0^{\frac{1}{2}d_p} \int_0^{2\pi} \left[\sqrt{K} \left(\frac{1}{2} d_p - r \right) + t \right] \cdot r\, d\theta\, dr\, dt , \qquad (4)$$

349 where r, θ and t define a cylindrical coordinate system, and t_s denotes the thickness of the scaffold.

350 Combining Equations (1), (2) and (4), $L_{bilayer}$ is expressed as:

$$351 \qquad L_{bilayer} = \frac{1}{24}\pi\left(\sqrt{K}d_p^3 t_s + 3t_s^2 d_p^2\right). \qquad (5)$$

352　It is called the equivalent diffusion path because the diffusivity difference between Li-in-NMC

353　and Li-in-LLZO is considered, and the diffusion path length in NMC to normalized by calculating

354　its equivalent length in LLZO.

355　　　　To consider a cell in which only a dense LLZO film and a dense layer of active material

356　are used, assuming the thickness of LLZO film and amount of NMC active material are the same

357　as used in the bilayer structure, the thickness of the active material layer is $t_a = P \cdot t_s$, and in this

358　situation the total equivalent diffusion path length L_{dense} is calculated to be:

$$359 \qquad L_{dense} = \int_{t_s}^{t_a+t_s} \int_0^{\frac{1}{2}(d_p+d_w)} \int_0^{2\pi} \left(t_s + \sqrt{K}t\right)\cdot rd\theta drdt = \frac{1}{8}\pi d_p^2 t_s^2\left(2\sqrt{K}+\sqrt{K}P+2\right) \qquad (6)$$

360　　　　To compare the equivalent diffusion path lengths of porous and dense LLZO films, the

361　$L_{bilayer}$ to L_{dense} ratio is computed to be

$$362 \qquad \frac{L_{dense}}{L_{bilayer}} = \frac{3t_s\left(\sqrt{K}P+2+2\sqrt{K}\right)}{\sqrt{K}d_p+3t_s}. \qquad (7)$$

363　　　　In most cases, the pore diameter d_p is much smaller than thickness of the scaffold t_s. Thus,

364　the ratio is approximated to be:

$$365 \qquad \frac{L_{dense}}{L_{bilayer}} = 2\sqrt{K}+2+\sqrt{K}P. \qquad (8)$$

366　　　　From this point of view, the higher the porosity is in the porous structure, the better the

367　performance that can be obtained, and the faster the diffusion is in LLZO compared to the active

368　materials, the more enhancement can be achieved. With NMC particles infiltrated in the LLZO

369　scaffold, K can be estimated to be about 10, according to the reported Li ion diffusivity around

370　10^{-10} cm^2/s in NMC[49] and 10^{-9} cm^2/s in LLZO[50]. Since porosity P ranges between 0 and 0.91, the

371   equivalent diffusion path length of the bilayer structure is 88% to 91% shorter than that of the

372   dense LLZO for Li ions. Although there is considerable variation for the literature values of Li ion

373   diffusivities in LLZO[50-53] and NMC[49, 54-56] it is still true that the equivalent diffusion path length

374   of the bilayer structure is much shorter than that of the dense LLZO configuration.

375   In practice, this will be highly dependent upon how intimately the active material and

376   LLZO contact each other, and will require careful optimization of the fabrication parameters. Thus

377   a dimensionless quantity, $A_{contact}$, which is defined as the contact area per unit LLZO film cross-

378   sectional area, is calculated by summing up the contribution from two parts – the base A_b and the

379   side-walls A_w:

$$A_{contact} = A_b + A_w = \frac{1}{4} N \pi d_p^2 + N \pi d_p t_s . \tag{9}$$

381   Substituting Equations (2) and (3) into (9), we get:

$$A_{contact} = P + \frac{4 P t_s}{d_p} . \tag{10}$$

383   From Equation (10), it is apparent that the diameter of the channels should be as small as

384   possible to increase contact area, but also that the porosity should be as high as possible. To

385   decrease the channel diameter, lower cooling temperatures and higher solidification rates in the

386   freeze casting experiment are preferred. However, as revealed in the experimental study, higher

387   freezing rates also decrease the wall thickness. Moreover, the wall thickness thinning rate is

388   usually slower than the channel diameter shrinking rate, resulting in lower porosity, which is not

389   desirable in terms of battery capacity, diffusion path length, and contact area. Therefore, it is not

390   useful to tune the microstructure by changing the cooling rate only. To obtain small pore diameter

391   and high porosity simultaneously, the LLZO slurry mass loading has to be decreased as well.

392   It must be emphasized that the model presented above primarily considers the Li ion

393   diffusion path length. However, in reality, more factors may need to be taken into account. Charge

394   transfer occurs at the cathode/LLZO interface during cell cycling and the kinetics will have a

395   strong impact on the performance of the cell. Besides contact area, the selection and matchup of

396   the morphology and size of the active material particles with respect to the pores in the LLZO

397   films are equally important. Large active material particles are more difficult to infiltrate into the

398   pores and channels and may result in relatively fewer points of contact between active material

399   and LLZO than if smaller particles are used. However, if small particles are infiltrated into pores

400   much larger than their diameters, there will also be particle-to-particle charge transfer resistance.

401   Moreover, volume changes during redox processes will affect the amount of contact among all the

402   components in the composite, and, thus the electrochemistry.

403

404   **Conclusion:**

405   Here we propose a novel configuration for thick composite electrodes in solid-state

406   batteries utilizing a freeze casting approach to make ionically conductive porous scaffolds, which

407   are then infiltrated with active material and other components. To illustrate the principle, we

408   prepared scaffolds using LLZO and TBA as the solvent. By changing the cooling bed temperature

409   and thus the solidification rate, the porosities and channel diameters can be varied. Sintering then

410   strengthens the structure and densifies the pore walls. 3D models of the LLZO scaffolds and

411   longitudinal sections were examined using monochromatic SR-μCT, and show that the low-

412   tortuosity channels are uniformly distributed parallel to the thickness of the scaffold, with pore

413   diameters almost constant from top to bottom. The open and oriented channels with few bridges

414   make it possible for large commercial cathode particles to be infiltrated into the structure readily.

415   As an example, a composite NMC622/LLZO electrode was successfully cycled in a hybrid cell

416   configuration. Bilayer structures were also fabricated by co-sintering a dense layer and a porous

417   layer together. SR-µXRF shows that the porous layer was successfully infiltrated with active

418   material. It was possible to read an open circuit potential on a totally solid state half cell consisting

419   of a lithium anode and the infiltrated bilayer structure. Theoretical calculations were performed to

420   model the porosity of the scaffolds, indicating that the porosity cannot exceed 91%. Higher

421   porosity results in higher energy density and should result in improved rate capability, by offering

422   shorter diffusion path lengths and larger contact areas. However, smaller channel diameters result

423   in increased contact area between the ionic conductor and active material, which also benefits

424   performance. While lowering the temperature of the freeze casting experiment results in smaller

425   pore sizes, it also decreases porosity. With these design considerations in mind, it is suggested that

426   the loading of LLZO in slurries for freeze casting experiments should be lowered to meet the

427   simultaneous goals of increased porosity and smaller pores.

428

429   **Acknowledgements**

454

References

456   1. J. Zheng, M. H. Engelhard, D. Mei, S. Jiao, B. J. Polzin, J.-G. Zhang and W. Xu, *Nat.*

457   *Energy*, 2017, **2**, 17012.

458   2. D. Deng, *Energy Sci. Eng.*, 2015, **3**, 385-418.

459   3. D. Lin, Y. Liu and Y. Cui, *Nat. Nanotechnol.*, 2017, **12**, 194-206.

460   4. P. Bai, J. Li, F. R. Brushett and M. Z. Bazant, *Energy Environ. Sci.*, 2016, **9**, 3221-3229.

461   5. C. Ma, Y. Cheng, K. Yin, J. Luo, A. Sharafi, J. Sakamoto, J. Li, K. L. More, N. J.

462   Dudney and M. Chi, *Nano Lett.*, 2016, **16**, 7030-7036.

463   6. Y. Zhu, X. He and Y. Mo, *J. Mater. Chem. A*, 2016, **4**, 3253-3266.

464   7. W. D. Richards, L. J. Miara, Y. Wang, J. C. Kim and G. Ceder, *Chem. Mater.*, 2015, **28**,

465   266-273.

466   8. J. Wolfenstine, J. L. Allen, J. Read and J. Sakamoto, *J. Mater. Sci.*, 2013, **48**, 5846-5851 .

467   9. T. Thompson, A. Sharafi, M. D. Johannes, A. Huq, J. L. Allen, J. Wolfenstine and J.

468   Sakamoto, *Adv. Energy Mater.*, 2015, **5**, 1500096.

469   10. R. Murugan, V. Thangadurai and W. Weppner, *Angew. Chem.*, 2007, **119**, 7925-7928.

470   11. A. Sharafi, H. M. Meyer, J. Nanda, J. Wolfenstine and J. Sakamoto, *J. Power Sources*,

471   2016, **302**, 135-139.

472   12. S. Yu, R. D. Schmidt, R. Garcia-Mendez, E. Herbert, N. J. Dudney, J. B. Wolfenstine, J.

473   Sakamoto and D. J. Siegel, *Chem. Mater.*, 2016, **28**, 197-206.

474   13. D. Rettenwander, G. Redhammer, F. Preishuber-Pflugl, L. Cheng, L. Miara, R. Wagner,

475   A. Welzl, E. Suard, M. M. Doeff, M. Wilkening, J. Fleig and G. Amthauer, *Chem.*

476   *Mater.*, 2016, **28**, 2384-2392.

477   14. L. Buannic, B. Orayech, J.-M. López Del Amo, J. Carrasco, N. A. Katcho, F. Aguesse,

478   W. Manalastas, W. Zhang, J. Kilner and A. Llordés, *Chem. Mater.*, 2017, **29**, 1769-1778.

479   15. Z. Zhang, Y. Shao, B. V. Lotsch, Y.-S. Hu, H. Li, J. Janek, C. Nan, L. Nazar, J. Maier,

480   M. Armand and L. Chen, *Energy Environ. Sci.*, 2018, **11**, 1945-1976.

481   16. K. Fu, Y. Gong, G. T. Hitz, D. W. McOwen, Y. Li, S. Xu, Y. Wen, L. Zhang, C. Wang,

482   G. Pastel, J. Dai, B. Liu, H. Xie, Y. Yao, E. D. Wachsman and L. Hu, *Energy Environ.*

483   *Sci.*, 2017, **10**, 1568-1575.

484   17. X. Han, Y. Gong, K. Fu, X. He, G. T. Hitz, J. Dai, A. Pearse, B. Liu, H. Wang, G.

485   Rubloff, Y. Mo, V. Thangadurai, E. D. Wachsman and L. Hu, *Nat. Mater.*, 2016, **16**, 572.

486   18. L. Porz, T. Swamy, B. W. Sheldon, D. Rettenwander, T. Frömling, H. L. Thaman, S.

487   Berendts, R. Uecker, W. C. Carter and Y.-M. Chiang, *Adv. Energy Mater.*, 2017, **7**,

488   1701003.

489   19. F. Shen, M. B. Dixit, X. Xiao and K. B. Hatzell, *ACS Energy Lett.*, **3**, 1056-1061.

490   20. H. Shen, E. Yi, L. Cheng, M. Amores, G. Chen, S. Sofie and M. Doeff, *Sust. Energy*

491   *Fuels*, 2019, DOI: 10.1039/C9SE00119K.

492   21. M. Kotobuki, H. Munakata, K. Kanamura, Y. Sato and T. Yoshida, *J. Electrochem. Soc.*,

493   2010, **157**, A1076-A1079.

494   22. J. van den Broek, S. Afyon and J. L. M. Rupp, *Adv. Energy Mater.*, 2016, **6**, 1600736.

495   23. E. Dumont-Botto, C. Bourbon, S. Patoux, P. Rozier and M. Dolle, *J. Power Sources*, **196**,

496   2274-2278.

497   24. G. Delaizir, V. Viallet, A. Aboulaich, R. Bouchet, L. Tortet, V. Seznec, M. Morcrette, J.-

498   M. Tarascon, P. Rozier and M. Dollé, *Adv. Funct. Mater.*, 2012, **22**, 2140-2147.

499   25. X. Yao, N. Huang, F. Han, Q. Zhang, H. Wan, J. P. Mwizerwa, C. Wang and X. Xu, *Adv.*

500   *Energy Mater.*, 2017, **7**, 1602923.

501   26. Yao, D. Liu, C. Wang, P. Long, G. Peng, Y. S. Hu, H. Li, L. Chen and X. Xu, *Nano Lett.*,

502   2016, **16**, 7148-7154.

503   27. Q. Zhang, H. Wan, G. Liu, Z. Ding, J. P. Mwizerwa and X. Yao, *Nano Energy*, 2019, **57**,

504   771-782.

505   28. K. Fu, Y. Gong, B. Liu, Y. Zhu, S. Xu, Y. Yao, W. Luo, C. Wang, S. D. Lacey, J. Dai, Y.

506   Chen, Y. Mo, E. Wachsman and L. Hu, *Sci. Adv.*, 2017, **3**, e1601659.

507   29. J. S. Sander, R. M. Erb, L. Li, A. Gurijala and Y. M. Chiang, *Nat. Energy*, 2016, **1**,

508   16099.

509   30. D. W. McOwen, S. Xu, Y. Gong, Y. Wen, G. L. Godbey, J. E. Gritton, T. R. Hamann, J.

510   Dai, G. T. Hitz, L. Hu and E. D. Wachsman, *Adv. Mater.*, 2018, **30**, e1707132.

511   31. M. B. Dixit, M. Regala, F. Shen, X. Xiao and K. B. Hatzell, *ACS Appl. Mater. Interfaces*,

512   2019, **11**, 2022-2030.

513   32. S. Deville, *Adv. Eng. Mater.*, 2008, **10**, 155-169.

514   33. L. Buannic, M. Naviroj, S. M. Miller, J. Zagorski, K.T. Faber and A. Llordes, *J. Am.*

515   *Ceram. Soc.*, 2019, **102**, 1021-1029.

516   34. E. Yi, W. Wang, J. Kieffer and R. M. Laine, *J. Mater. Chem. A*, 2016, **4**, 12947-12954.

517   35. D. Gursoy, F. De Carlo, X. Xiao, and C. Jacobsen, *J. Synchrotron Radiation*, 2014, **21**,

518   1188-1193.

519   36. R. J. Pandolfi, D. B. Allan, E. Arenholz, L. Barroso-Luque, S. I. Campbell, T. A.

520   Caswell, A. Blair, F. De Carlo, S. Fackler, A.P. Fournier, G. Freychet, M. Fukuto, D.

521   Gursoy, Z. Jiang, H. Krishnan, D. Kumar, R. J. Kline, R. Li, C. Liman, S. Marchesini, A.

522   Mehta, A. T. N'Diaye, D. Y. Parkinson, H. Parks,L.A. Pellouchoud, T. Perciano, F. Ren,

523   S. Sahoo, J. Strzalka, D. Sunday, C. J. Tassone, D. Ushizima, S. Venkatakrishnan, K. G.

524   Yager, P. Zwart, J. A. Sethian, and A. Hexemer, *J. Synchrotron Radiation*, 2018, **25**,

525   1261-1270.

526   37. T. Xu and C.-A. Wang, *Mater. Des.*, 2016, **91**, 242-247.

527   38. Z. Wu, S. Ji, Z. Hu, J. Zheng, S. Xiao, Y. Lin, K. Xu, K. Amine and F. Pan, *ACS Appl.*

528   *Mater. Interfaces*, 2016, **8**, 15361-15368.

529 39. Y. Ruan, X. Song, Y. Fu, C. Song and V. Battaglia, *J. Power Sources*, 2018, **400**, 539-
530   548.

531 40. E. Markevich, G. Salitra, F. Chesneau, M. Schmidt and D. Aurbach, *ACS Energy Lett.*,
532   2017, **2**, 1321-1326.

533 41. G. Salitra, E. Markevich, M. Afri, Y. Talyosef, P. Hartmann, J. Kulisch, Y. K. Sun and
534   D. Aurbach, *ACS Appl. Mater. Interfaces*, 2018, **10**, 19773-19782.

535 42. F. Lin, I. M. Markus, D. Nordlund, T. C. Weng, M. D. Asta, H. L. Xin and M. M. Doeff,
536   *Nat. Commun.*, 2014, **5**, 3529.

537 43. F. Lin, D. Nordlund, I. M. Markus, T.-C. Weng, H. L. Xin and M. M. Doeff, *Energy*
538   *Environ. Sci.*, 2014, **7**, 3077.

539 44. J. Zhu and G. Chen, *J. Mater. Chem. A*, 2019, **7**, 5463.

540 45. C. Tian, D. Nordlund, H. L. Xin, Y. Xu, Y. Liu, D. Sokaras, F. Lin and M. M. Doeff, *J.*
541   *Electrochem. Soc.*, 2018, **165**, A696-A704.

542 46. S.-K. Jung, H. Gwon, J. Hong, K.-Y. Park, D.-H. Seo, H. Kim, J. Hyun, W. Yang and K.
543   Kang, *Adv. Energy Mater.*, 2013, **4**, 1300787.

544 47. L. Zou, W. Zhao, Z. Liu, H. Jia, J. Zheng, G. Wang, Y. Yang, J.-G. Zhang and C. Wang,
545   *ACS Energy Lett.*, 2018, **3**, 2433-2440.

546 48. G. T. Hitz, D. W. McOwen, L. Zhang, Z. Ma, Z. Fu, Y. Wen, Y. Gong, J. Dai, T. R.
547   Hamann, L. Hu and E. D. Wachsman, *Mater. Today*, 2019, **22**, 50-57.

548 49. A. Einstein, Ann. d. Phys., 1905, **17**, 549-560.

549 50. P.-C. Tsai, B. Wen, M. Wolfman, M.-J. Choe, M. S. Pan, L. Su, K. Thornton, J. Cabana
550   and Y.-M. Chiang, *Energy Environ. Sci.*, 2018, **11**, 860-871.

551   51. M. Månsson, H. Nozaki, J. M. Wikberg, K. Prša, Y. Sassa, M. Dahbi, K. Kamazawa, K.

552   Sedlak, I. Watanabe and J. Sugiyama, *J. Phys. Conf. Ser.*, 2014, **551**, 012037.

553   52. M. Amores, T. E. Ashton, P. J. Baker, E. J. Cussen and S. A. Corr, *J. Mater. Chem. A*,

554   2016, **4**, 1729-1736.

555   53. K. Hayamizu, S. Seki and T. Haishi, *J. Chem. Phys.*, 2017, **146**, 024701.

556   54. C. Chen, Z. Lu and F. Ciucci, *Sci. Rep.*, 2017, **7**, 40769.

557   55. Y. Wei, J. Zheng, S. Cui, X. Song, Y. Su, W. Deng, Z. Wu, X. Wang, W. Wang, M. Rao,

558   Y. Lin, C. Wang, K. Amine and F. Pan, *J. Am. Chem. Soc.*, 2015, **137**, 8364-8367.

559   56. S. Cui, Y. Wei, T. Liu, W. Deng, Z. Hu, Y. Su, H. Li, M. Li, H. Guo, Y. Duan, W. Wang,

560   M. Rao, J. Zheng, X. Wang and F. Pan, *Adv. Energy Mater.*, 2016, **6**, 1501309.

561   57. S.-L. Wu, W. Zhang, X. Song, A. K. Shukla, G. Liu, V. Battaglia and V. Srinivasan, *J.*

562   *Electrochem. Soc.*, 2012, **159**, A438-A444.

563

564   **Figure captions**

565   Fig. 1 Schematics of (a) the freeze casting apparatus and (b) formation of the porous green body

566   by freeze drying. Insets are the bulk scaffold before and after sintering, with rulers serving as scale

567   bars. (c) shows slices cut from the sintered scaffold mounted in epoxy. A 200 μm thick slice is

568   transparent, as displayed in the lower part of (c).

569   Fig. 2 SEM images of the fractured LLZO scaffolds (a-b) before and (c-d) after sintering.

570   Fig. 3 The 3D reconstructed structure from the SR-μCT data of (a) the LLZO film and (b)

571   longitudinal section. The cross sections for the film are shown in (b) top and (c) left views. (e) and

572   (f) are the top and left views of the LLZO longitudinal section.

573   Fig. 4 SEM top views of the sintered LLZO scaffolds, frozen at -20 °C and -50 °C, respectively, at

574   low and high magnifications.

575   Fig. 5 (a) XRD pattern of the scaffold after sintering and after epoxy removal, respectively. The

576   LLZO XRD peaks are indicated in the lower part. (b) is the SEM image of the scaffold flipped

577   over after drop casting of NMC particles from the other side.

578   Fig. 6 (a) The cycling curves, (b) capacity and columbic efficiency, and (c) impedance curves of

579   the hybrid cell from the 1st to the 90th cycle.

580   Fig. 7 (a) Schematic of the bilayer fabrication. Inset shows a bilayer structure on graphite, with

581   carbon left on the top surface after sintering. The porous scaffold and dense film XRD patterns are

582   displayed in (b). Fractured bilayer structure with (c) thick and (d) thin dense films are presented.

583   The SEM backscattered electron image (e) and its synchrotron radiation X-ray fluorescence maps

584   (f) of the infiltrated bilayer structure indicate well-distributed NMC particles in areas where LLZO
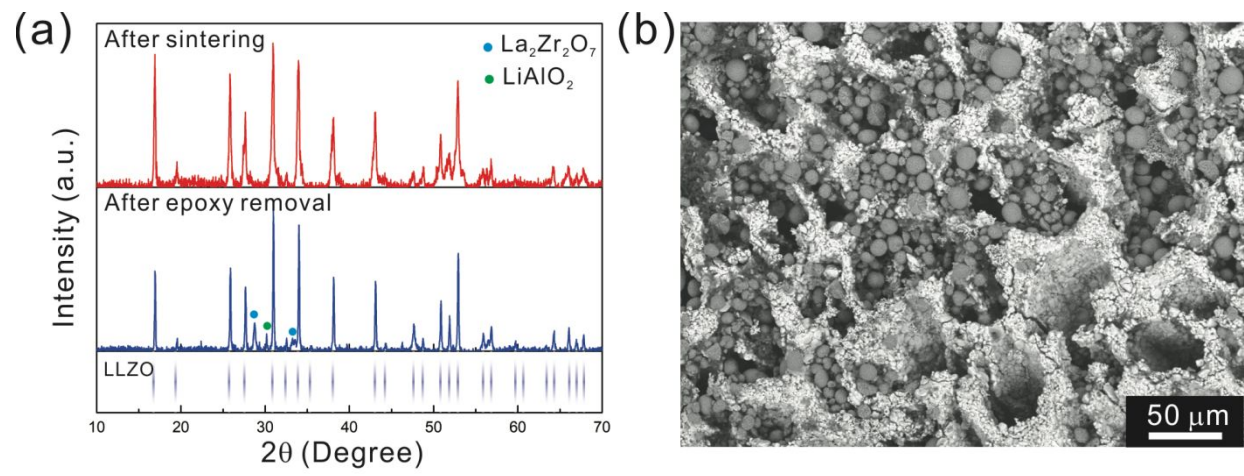
585   is absent.

586   Fig. 8 (a) The 3D model and (b) top view of the simplified honeycomb structure of the porous

587   LLZO scaffold.

Figure 1

Figure 2

29
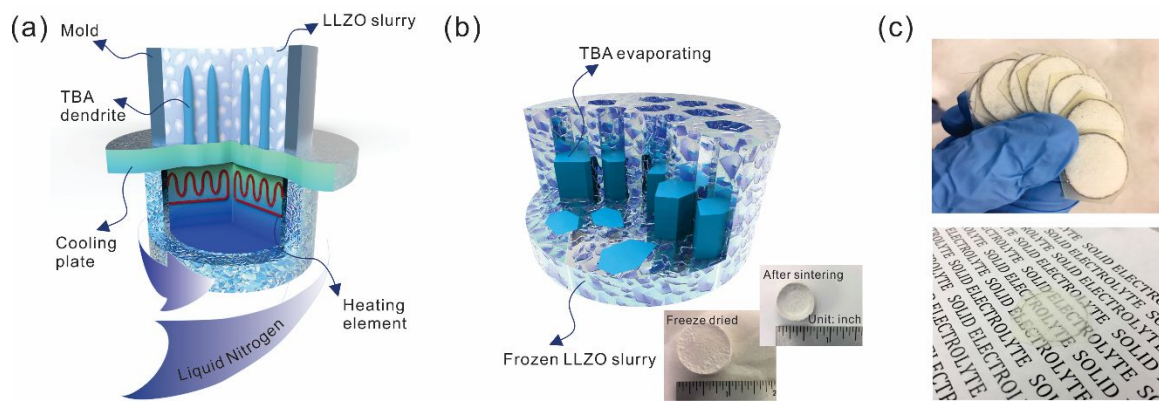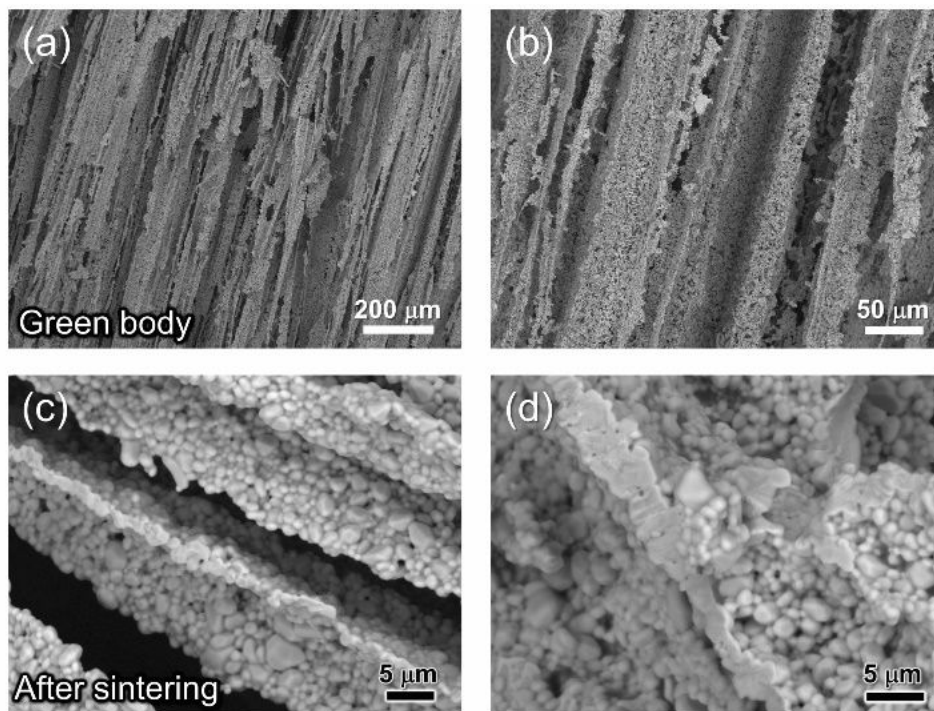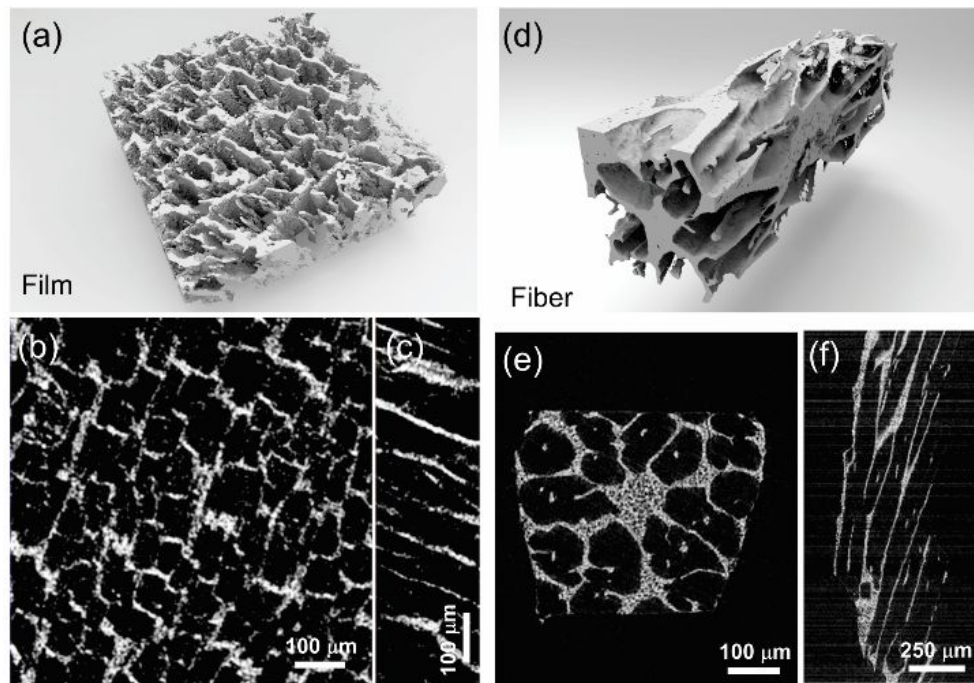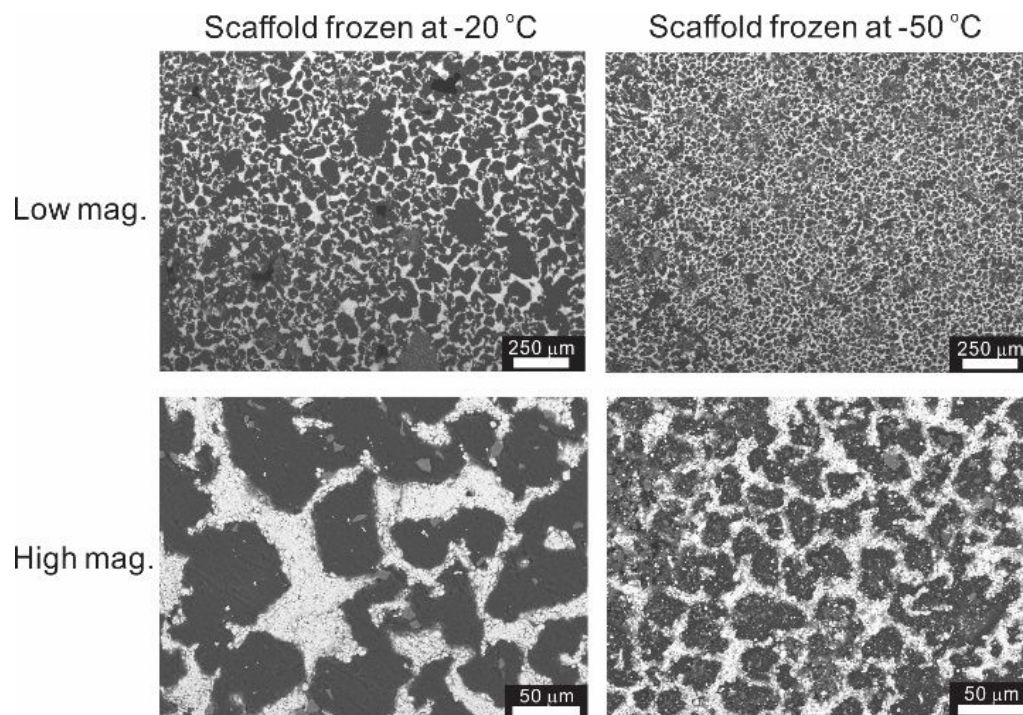
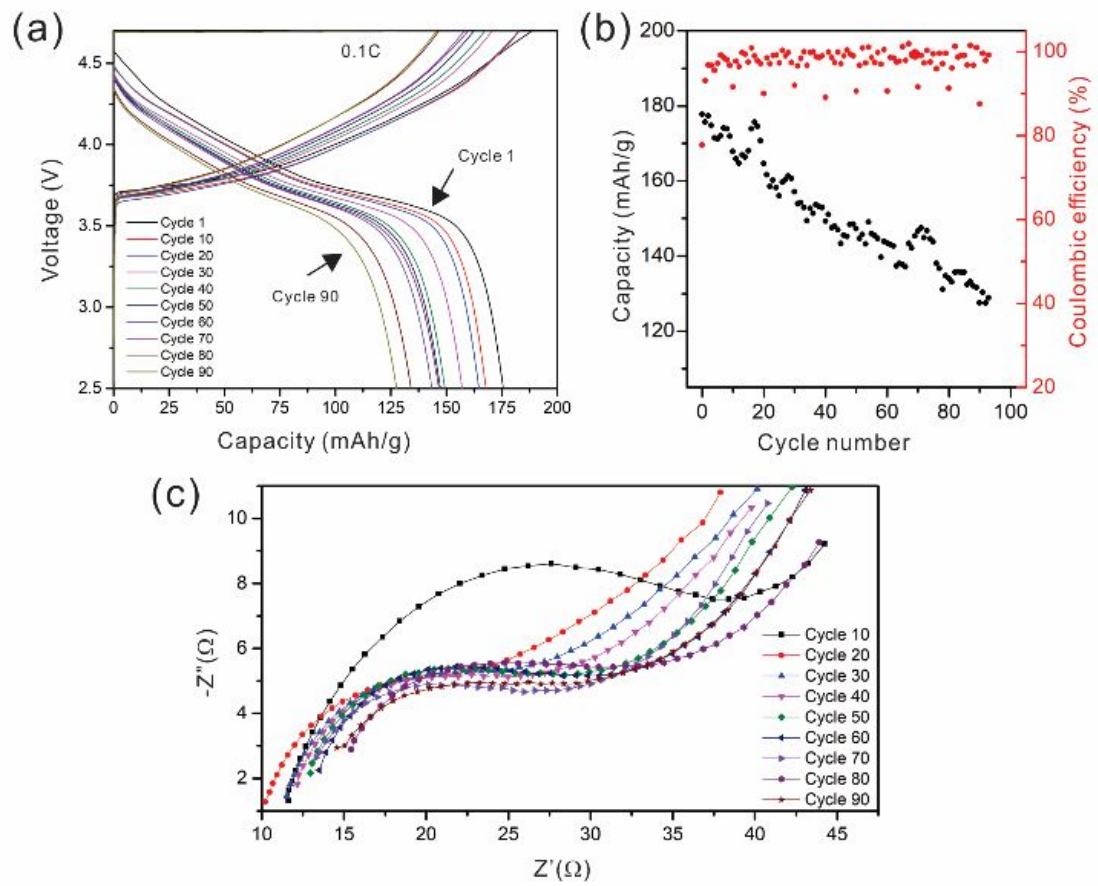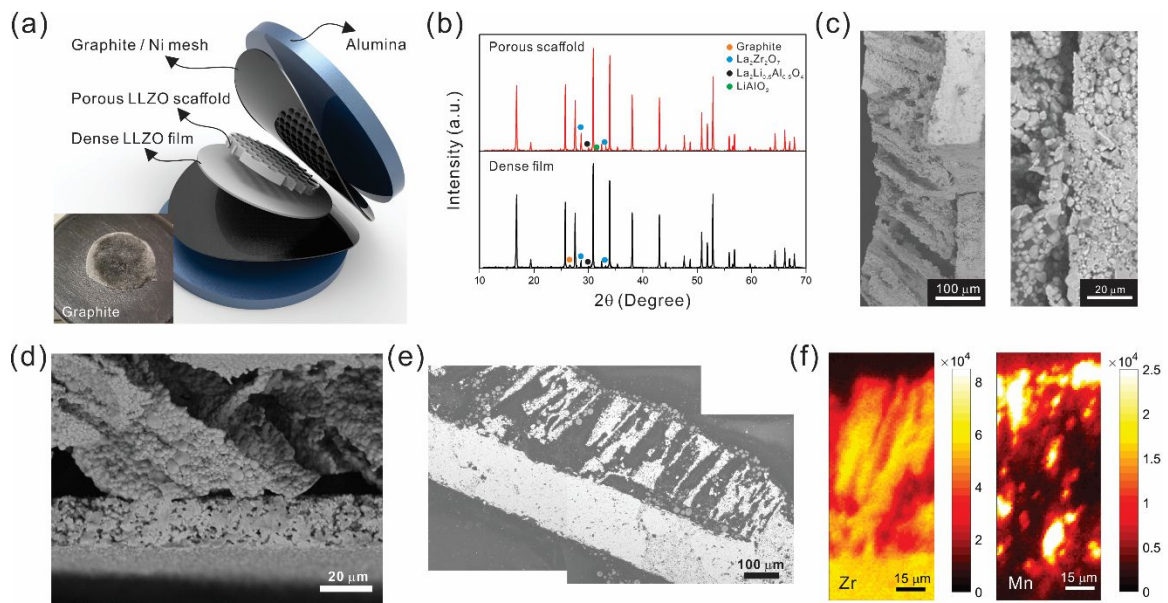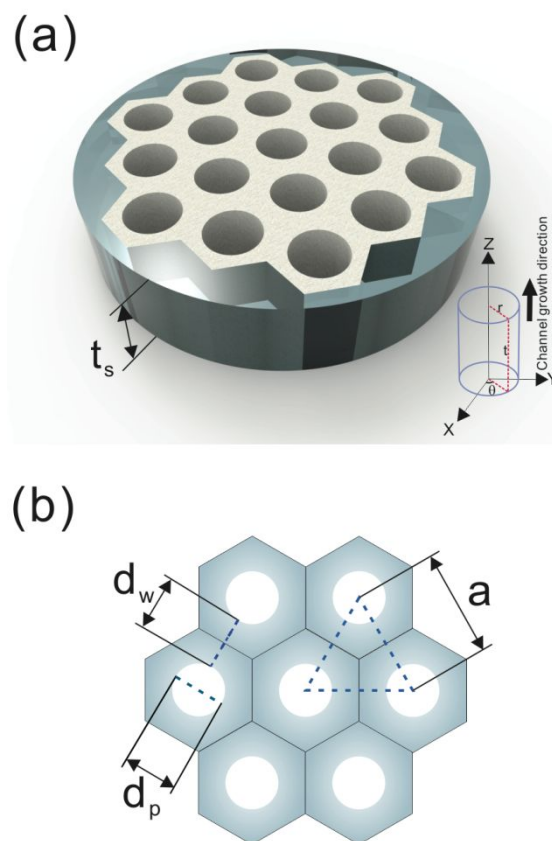**Figure 3**

Figure 4

Figure 5

Figure 6

Figure 7

Figure 8